

Progress Report on Phase Separation in Polymer Solutions

Fei Wang,* Patrick Altschuh,* Lorenz Ratke, Haodong Zhang, Michael Selzer, and Britta Nestler

Polymeric porous media (PPM) are widely used as advanced materials, such as sound dampening foams, lithium-ion batteries, stretchable sensors, and biofilters. The functionality, reliability, and durability of these materials have a strong dependence on the microstructural patterns of PPM. One underlying mechanism for the formation of porosity in PPM is phase separation, which engenders polymer-rich and polymer-poor (pore) phases. Herein, the phase separation in polymer solutions is discussed from two different aspects: diffusion and hydrodynamic effects. For phase separation governed by diffusion, two novel morphological transitions are reviewed: “cluster-to-percolation” and “percolation-to-droplets,” which are attributed to an effect that the polymer-rich and the solvent-rich phases reach the equilibrium states asynchronously. In the case dictated by hydrodynamics, a deterministic nature for the microstructural evolution during phase separation is scrutinized. The deterministic nature is caused by an interfacial-tension-gradient (solutal Marangoni force), which can lead to directional movement of droplets as well as hydrodynamic instabilities during phase separation.

which produces porous layers with adjustable properties. As the porosity is established by the introduced pores, there exist strong correlations between the resulting specific surface area, the volume fraction, and the size distribution of pores as essential properties. Depending on the constellation of the properties, PPM with beneficial capabilities, such as permeability, particle retention as well as acoustic and thermal insulation effects are realized with pores sizes at different length scales ranging from nanometer to millimeter. The pore sizes of PPM are categorized according to the International Union of Pure and Applied Chemistry (IUPAC) recommendation into three groups:^[2] macropores (pore size > 50 nm), mesopores (pore size = 2–50 nm), and micropores (pore size < 2 nm) where a porosity varying from 20% to 90% is attainable.

1. Introduction

Polymeric porous media (PPM) have received an increased level of interest over recent decades,^[1] not least because PPM fulfill tasks where alternatives are technically and economically impractical.^[2] The success story of PPM originates from the concept of introducing pores into a dense polymer matrix in a controlled fashion,


Since the way of introducing pores into polymers has been investigated for many years now, a large number of formation processes thrive on both industrial and academic fields. Commercially relevant methods^[3] include tearing, foaming, self-assembling templates, track edge, weaving, polymer mixing, and block copolymers, covalent organic frameworks, and phase separation where the last one is the focus of this review. In academia, another method is proposed based on the pore formation through templating. Herein, the polymer grows around a template matrix which could be a solid (hard templating),^[3] an emulsion (emulsion templating),^[4] or a dispersed gaseous phase (foam templating),^[5] to name a few. As a result, the intrinsic properties of the template are inherited to the PPM. Since in general, purely synthetic polymers are used, the controllability of the formation processes is promoted and a broad range of pore sizes can be achieved.^[3]

While in earlier days of engineering materials, the avoidance of porosities was the main objective,^[6] in PPM it is explicitly utilized to provoke the aforementioned beneficial capabilities of the polymer materials and to facilitate versatile and momentous applications.^[1] For instance, PPM shows its extraordinary efficiency in various membrane separation processes^[7] where a transmembrane gradient forces a fluid to pass the porous membrane through the pores and particles are filtered by the physical principle of size exclusion.^[2] Very commonly, these processes are widely used for purifying water by removing pollutants (e.g., agricultural chemicals, endocrine disruptors, pathogens) on distinct length scales (e.g., nano-, ultra-, and microfiltration).^[8,9] During the purification, a pressure gradient is imposed on wastewater, whereas in dialysis, the separation

Dr. F. Wang, P. Altschuh, H. Zhang, Dr. M. Selzer, Prof. B. Nestler
Institute of Applied Materials-Computational Materials Science
Karlsruhe Institute of Technology (KIT)
Straße am Forum 7, 76131 Karlsruhe, Germany
E-mail: fei.wang@kit.edu; patrick.altschuh@kit.edu

P. Altschuh, Dr. M. Selzer, Prof. B. Nestler
Institute of Digital Materials Science
Karlsruhe University of Applied Sciences
Moltkestraße 30, 76133 Karlsruhe, Germany

Prof. L. Ratke
Institute of Materials Research
German Aerospace Center (DLR)
Linder Hoehe, 51147 Cologne, Germany

 The ORCID identification number(s) for the author(s) of this article can be found under <https://doi.org/10.1002/adma.201806733>.

© 2019 Institute for Applied Materials-Computational Materials Science, Karlsruhe Institute of Technology. Published by WILEY-VCH Verlag GmbH & Co. KGaA, Weinheim. This is an open access article under the terms of the Creative Commons Attribution-NonCommercial License, which permits use, distribution and reproduction in any medium, provided the original work is properly cited and is not used for commercial purposes.

DOI: 10.1002/adma.201806733

is driven by a concentration gradient.^[10] Additional applications comprise biomaterials and lab-on-a-chip technologies including lateral flow assays, such as blood glucose analyzer^[11] and pregnancy tests,^[12,13] respectively. Furthermore, thanks to alterable ultrahigh surface areas, PPM have been adopted for catalyst supports to increase the efficiency of chemical reactions^[14,15] and for electrodes of lithium-ion battery to enhance the electrochemical performance.^[16–18] PPM have also been exploited for energy storage devices,^[19] fuel cells,^[20] low-dielectric-constant materials,^[21] photonic bandgap materials,^[22,23] scaffolds for tissue engineering,^[4] proton exchange membranes,^[24,25] masks for nanopatterning or lithography,^[26] antireflection coating,^[27] and many other applications. In these high-value applications, the functionality, the reliability, and the durability of PPM crucially depend on the microstructural patterns resulting from different formation processes associated with diverse underlying mechanisms.

One underlying mechanism for the formation of PPM is phase separation, which gives rise to a polymer-rich phase and a polymer-poor (pore) phase. **Figure 1a** lists a number of phase separation microstructures^[28–39] in different polymer solutions. The phase separation in polymer solutions is premised on the Flory–Huggins theory,^[40,41] according to which the Gibbs free energy of a polymer solution depends on the average degree of polymerization (DP). When the monomer (DP = 1) is dissolved in the solvent with a volume concentration ϕ , the Gibbs free energy $f(\phi)$ has a global minimum at $\phi = \phi_m$, as sketched by the dashed line in Figure 1b. Therefore, the system remains a homogeneous solution at the minimum energy state. When the polymerization, i.e., crosslinking reaction, takes place, the molecular weight of the polymerizing species progressively increases and thereby DP levels up. For sufficiently large DPs, two local minima occur in the free energy landscape $f(\phi)$, as depicted by the solid line in Figure 1b. In order to decrease the Gibbs free energy, the homogeneous polymer solution decomposes into two separate phases with concentrations around the two local minima.

Phase separation in polymer solutions involves not only diffusion but also hydrodynamic effects. From these two mass transport aspects, we give an overview of recently significant advances on the microstructural evolution of phase separation in polymer solutions. For diffusion-governed evolutions, two novel morphological transitions: “cluster-to-percolation” and “percolation-to-droplets” are elucidated. These new morphological transitions are caused by the fact that the polymer-rich and the solvent-rich phases reach the equilibrium states asynchronously, which is attributed to the highly asymmetrical phase diagram of polymer solutions. Given that the asynchronous effect is affected not only by the thermodynamic driving force but also by the mobility, we give an overview of some recent progress on the development of the mobility and point out some insight into constructing the mobility in future works, as an open question.

For phase separation involving hydrodynamic effects, an up-to-date work from Shimizu and Tanaka^[42] is described. This work reveals a fundamental understanding that the motion of the droplets resulting from phase separation is a deterministic rather than a stochastic behavior. Concretely speaking, the motion of droplets is directional, contrary to the Brownian motion mechanism where stochastic thermal forces exerted by molecules induce random motion of individual droplets. This deterministic nature



Fei Wang is a research scientist at Karlsruhe Institute of Technology (KIT). His interests span a wide range of fields including phase separation in polymers and metals, solidification, fluid dynamics, wetting, and phase-field modeling. He completed his Ph.D. in the department of mechanical engineering at KIT in 2017.



Patrick Altschuh is a research assistant and Ph.D. student at Karlsruhe Institute of Technology (KIT). His research interests include computational characterization techniques, fluid dynamics, and multiscale modeling approaches, which are applied for microfluidics in porous media as well as membrane separation processes. He received his M.Sc. from Karlsruhe University of Applied Sciences in mechanical engineering.



Britta Nestler is a full professor for microstructure simulation in materials science at Karlsruhe Institute of Technology (KIT), director of the Institute of Applied Materials at KIT and the Institute of Digital Materials Science at Karlsruhe University of Applied Sciences. She pursues research in multi-physics materials modeling and high-performance materials simulations.

is engendered by an interfacial tension gradient (Marangoni force) produced in each droplet as a consequence of composition correlation among droplets. In order to reduce the total surface energy, the droplets move from a high surface tension to a low surface tension region, giving rise to a directional movement. The interfacial tension gradient not only drives the directional motion of droplets but also expedites a hydrodynamic instability at a fluid–fluid interface during phase separation,^[43] which will be summarized as well.

Phase separation in polymer solutions results in complicated porous patterns involving complex physical mechanisms behind. To deeply understand the hidden mechanisms, it is strongly demanded to develop effective characterization

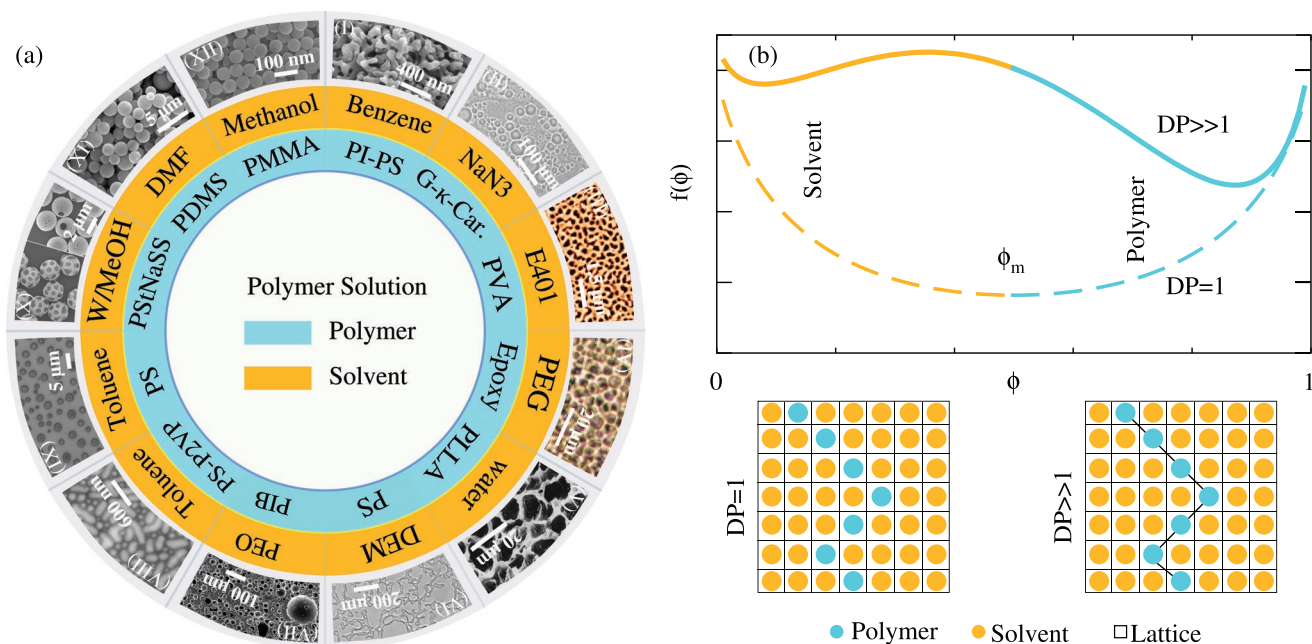


Figure 1. a) The blue, yellow, and gray rings represent, respectively, the polymer, the solvent and the porous structures due to phase separation. I) Reproduced with permission.^[28] Copyright 2006, American Chemical Society; II) Reproduced with permission.^[29] Copyright 2000, Elsevier; III) Reproduced with permission.^[30] Copyright 2012, Royal Society of Chemistry; IV) Reproduced with permission.^[31] Copyright 2014, American Chemical Society; V) Reproduced with permission.^[32] Copyright 1996, Wiley-VCH; VI) Reproduced with permission.^[33] Copyright 2006, Elsevier; VII) Reproduced with permission.^[34] Copyright 2017, American Institute of Physics; VIII) Reproduced with permission.^[35] Copyright 2017, MDPI; IX) Reproduced with permission.^[36] Copyright 2005, Springer Nature; X) Reproduced with permission.^[37] Copyright 2017, Royal Society of Chemistry; XI) Reproduced with permission.^[38] Copyright 2005, American Chemical Society; XII) Reproduced with permission.^[39] Copyright 2016, The Korean Ceramic Society. b) Free energy landscape of polymer solutions with an average degree of polymerization (DP) equal to 1 (dashed line) and much greater than 1 (solid line). The free energy density $f(\phi)$ has two contributions: enthalpy and entropy. The former one is proportional to $\phi(1 - \phi)$, which is concave downward. The convexity of the free energy landscape is controlled by the enthalpy $\phi \ln \phi / DP$. When $DP = 1$, the homogeneously distributed monomers in the solvent correspond to a high entropy state, whose free energy density is convex. As $DP \gg 1$, long polymer chains are formed and the entropy contribution becomes less eminent, which gives rise to a double-well free energy density. PS, polystyrene (atactic); PI, polyisoprene; NaN_3 , sodium azide; G- κ -Car., Gellan- κ -carrageenan; PEG, poly(ethylene glycol); E401, sodium alginate; PVA, poly(vinyl alcohol); PLLA, poly(lactic acid); DEM, diethyl malonate; PEO, poly(ethylene oxide); PIB, polyisobutylene; PS-P2VP, poly(styrene-*b*-2 vinyl pyridine); PStNaSS, polystyrene-sodium sulfonate styrene; MeOH, methyl alcohol; PDMS, poly(dimethylsiloxane); DMF, dimethylformamide; W, water.

techniques to scrutinize the phase separation patterns. The commonly applied characterization methods are very different in their operating length scales. Experimental methods, such as capillary flow pyrometry, specific surface area studied by nitrogen adsorption using the Brunauer–Emmett–Teller (BET) method, and water permeability, are conducted on a macroscopic scale. By employing simplified theoretical models from Young–Laplace, Fick and Darcy, effective properties are extracted, but no concrete information about the morphologies of the microstructures is accessible. Not surprisingly, the respective concepts have many limitations and the material behaves rather like a “black box.” In contrast, computational materials science provides powerful opportunities for characterizing the microstructures on the pore-scale by combining computer-aided characterization methods and digital representations of the microstructure. As such, we give an overview of a novel characterization method for porous microstructures.

Herein, in Section 2, we review the-state-of-the-art phase-field model which is used to explore the novel microstructural evolution mechanisms reported in the following sections. In Section 3, we provide a general background of physical pictures for diffusion and hydrodynamic effect. In Section 4, we elucidate two new

morphological transitions governed by diffusion. In Section 5, we describe a deterministic nature for the microstructural evolution arising from hydrodynamic effects. Thereafter, an insightful method for the characterization of porous microstructures is introduced in Section 6. We conclude the report at the last section.

2. The-State-of-the-Art Phase-Field Model to Simulate Phase Separation in Polymer Solutions

The free energy density of a polymer solution is formulated by the Flory–Huggins theory,^[40] which is a lattice based model, as sketched in **Figure 2a**.^[44] By modifying the entropy of regular solutions, the free energy density depends on the average degree of polymerization N and is expressed in terms of the polymer concentration ϕ and the temperature T by

$$f(\phi, T) = k_b T \left[\frac{\phi}{N} \ln \phi + (1 - \phi) \ln(1 - \phi) + \chi \phi(1 - \phi) \right] \quad (1)$$

Here, k_b denotes the Boltzmann constant and χ represents the Flory parameter. For an upper critical point spinodal

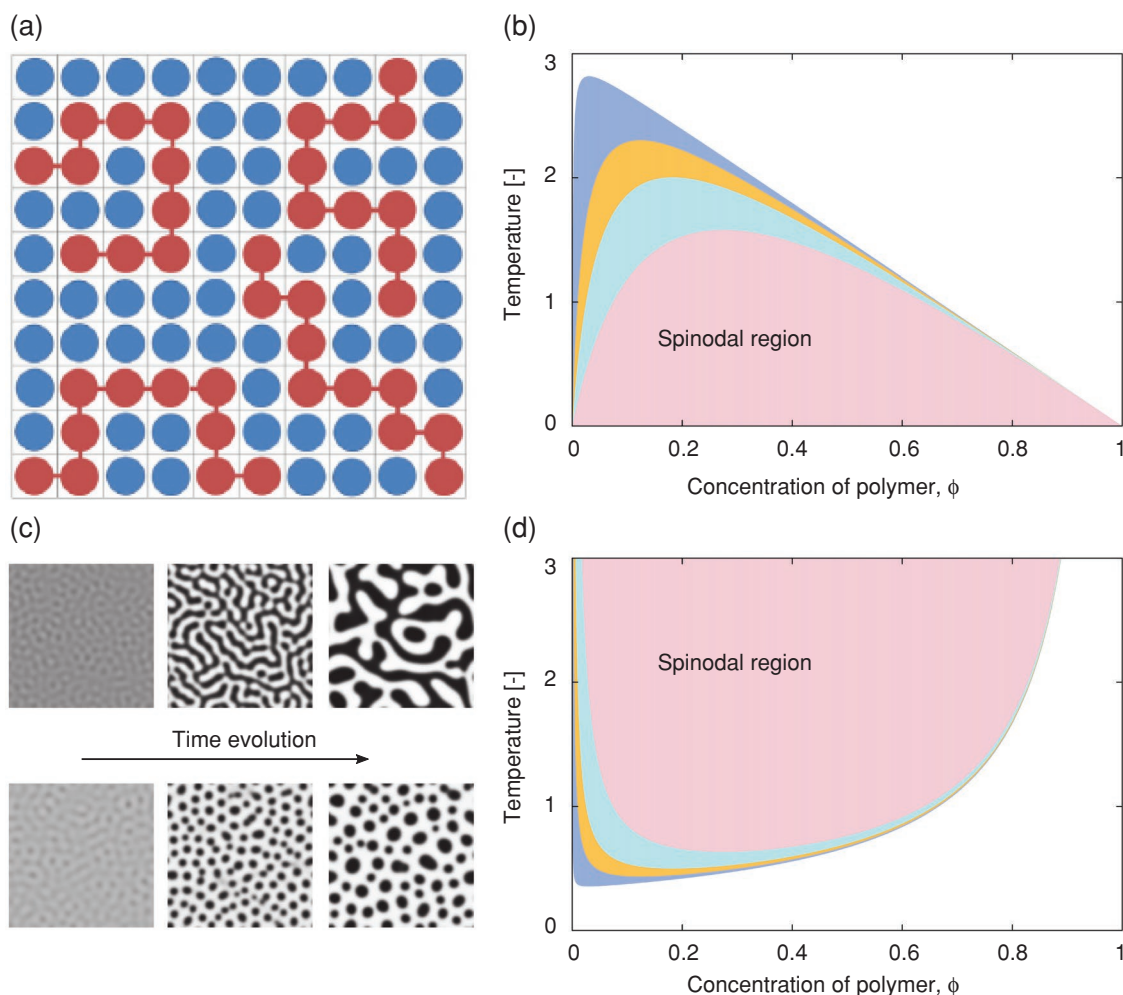


Figure 2. Flory–Huggins theory and the phase diagram: a) Sketch for the lattice-based model of Flory–Huggins. The red and blue circles represent the polymer and solvent species, respectively. Reproduced with permission.^[44] Copyright 2016, Elsevier. b) Reproduced spinodal regions for an upper critical point system from the Flory–Huggins theory. Distinct colored areas correspond to different average degrees of polymerization (red: $N = 7$, green: $N = 20$, orange: $N = 50$, blue: $N = 1000$). c) Formation of bicontinuous and droplet structures due to spinodal decomposition with concentrated (upper) and dilute (bottom) initial polymer solutions. c) Reproduced with permission.^[33] Copyright 2006, Elsevier. d) Spinodal regions for a lower critical point system.

decomposition (UCSD), the Flory parameter is inversely proportional to the temperature $\chi = Z\Delta\epsilon/k_bT$, where Z is a coordination number and $\Delta\epsilon$ is the difference of the bond energy between polymer–solvent ϵ_{PS} and the average value of polymer–polymer ϵ_{PP} and solvent–solvent ϵ_{SS} , namely, $\Delta\epsilon = \epsilon_{PS} - (\epsilon_{PP} + \epsilon_{SS})/2$. When $\Delta\epsilon$ is positive, the polymer–polymer and the solvent–solvent bonds are energetically favored rather than the polymer–solvent bond of a homogeneous mixture. For a lower critical point spinodal decomposition (LCSD), the Flory parameter is linearly proportional to the temperature, $\chi \sim T$.

The spinodal line is calculated by the locus of $\partial^2 f / \partial \phi^2 = 0$. The binodal line is given by the conditions: i) $\mu_p := \partial_\phi f|_{\phi=\phi_p} = \partial_\phi f|_{\phi=\phi_s} =: \mu_s$ and ii) $(f - \mu_p \phi)|_{\phi=\phi_p} = (f - \mu_s \phi)|_{\phi=\phi_s}$. Here, ϕ_p and ϕ_s are the equilibrium polymer concentrations in the polymer-rich and the polymer-poor phases, respectively, and μ_p and μ_s stand for the corresponding equilibrium chemical potentials. Since the average degree of polymerization N is a time dependent parameter, $N = 1 + kt^{[45,46]}$ with k being a reaction-rate constant, it is noted that the spinodal as well as

the binodal lines both are dynamic. Figure 2b,d reproduce the spinodal lines for a series of DPs (red: $N = 7$, green: $N = 20$, orange: $N = 50$, blue: $N = 1000$) with a Flory parameter $\chi = 1.5$ for UCSD and LCSD, respectively.

When the polymer concentration is initially set inside the spinodal region, the polymer solution spontaneously decomposes into two separate phases, known as spinodal decomposition (Figure 2c). In a closed system under isothermal and isobaric conditions, this decomposition is such as to reduce the free energy functional, which is expressed as^[47]

$$F(\phi, \nabla\phi) = \int_V [f(\phi) + \kappa(\nabla\phi)^2] dv \quad (2)$$

where V is the domain occupied by the system and κ denotes a gradient energy coefficient which is determined by the interfacial tension σ as $\kappa = \sigma / (2 \int_{-\infty}^{\infty} (d\phi/dx)^2 dx)$. The spinodal decomposition is computed by considering an uphill diffusion flux, $\mathbf{J} = -M(\phi)\nabla(\delta\mathcal{F}/\delta\phi)$, in the Cahn–Hilliard equation, reading^[48]

$$\partial_t \phi = \nabla \cdot [M(\phi) \nabla (\delta \mathcal{F} / \delta \phi)] \quad (3)$$

where $M(\phi)$ is the mobility.

We stress that for liquid phases, on spinodal decomposition the reduction of the free energy is achieved not only via diffusion but also via fluid flow or convection which transports kinetic energy $\frac{1}{2} \rho |\mathbf{u}|^2$. Here, ρ is the density and \mathbf{u} is the mean velocity of the fluid. Thus, the mass flux generally contains two contributions: one is diffusion arising from the chemical potential gradient and the other one is caused by convection $\phi \mathbf{u}$ describing the transport via the mean velocity. With the generalized mass flux, $\mathbf{J} = -M(\phi) \nabla (\delta \mathcal{F} / \delta \phi) + \phi \mathbf{u}$, the mass conservation equation is rewritten as^[49]

$$\partial_t \phi + \nabla \cdot (\mathbf{u} \phi) = \nabla \cdot [M(\phi) \nabla (\delta \mathcal{F} / \delta \phi)] \quad (4)$$

The kinetic energy $\frac{1}{2} \rho |\mathbf{u}|^2$ has not been considered in the classic Cahn–Hilliard model, but is taken into account in recent works.^[50–54] On account of convection, a portion of the free energy is transformed into kinetic energy. The decrease rate of the Gibbs free energy caused by convection is $(d\mathcal{F}/dt)_{\text{convection}} = \int_V (\delta \mathcal{F} / \delta \phi) (\partial_t \phi)_{\text{convection}} dV$, which is equivalent to $-\int_V (\delta \mathcal{F} / \delta \phi) (\mathbf{u} \cdot \nabla \phi) dV$ by using the mass conservation equation and the incompressibility condition $\nabla \cdot \mathbf{u} = 0$. Equating the increase rate of the kinetic energy $\int_V \mathbf{f}_s \cdot \mathbf{u} dV$ to the decrease rate of the Gibbs free energy, the capillary force is derived, $\mathbf{f}_s = -\phi \nabla (\delta \mathcal{F} / \delta \phi)$.^[55] The derivation of the capillary force is actually in accordance with Noether's theorem that the action of a physical system is invariant to a specific transformation of the coordinates and field variables, yielding a stress tensor^[56,57]

$$\underline{\underline{\Theta}} = 2\kappa \nabla \phi \otimes \nabla \phi - (\kappa \nabla \phi \cdot \nabla \phi + f) \mathbf{I} \quad (5)$$

The tensorial formulation has been used in refs. [52,55,58]. It can be readily shown that $-\nabla \cdot \underline{\underline{\Theta}} = -\phi \nabla (\delta \mathcal{F} / \delta \phi)$ by using the equality $\nabla \cdot (\nabla \phi \otimes \nabla \phi) = \nabla^2 \phi \nabla \phi + (\nabla \phi \cdot \nabla) \nabla \phi$.

Including the capillary force in the Navier–Stokes equation, we obtain a generalized momentum balance equation^[55,68]

$$\rho (\partial_t \mathbf{u} + \mathbf{u} \cdot \nabla \mathbf{u}) = -\nabla p + \nabla \cdot \left\{ \left[\kappa (\nabla \phi)^2 + f \right] \mathbf{I} - 2\kappa \nabla \phi \otimes \nabla \phi \right\} + \nabla \cdot \eta (\nabla \mathbf{u} + \nabla \mathbf{u}^T) \quad (6)$$

where p , η , and \mathbf{I} are the pressure, the viscosity and the identity tensor, respectively. It is noted that Equation (6) is valid when the densities of the polymer-rich ρ_p and the solvent-rich ρ_s phases are nearly the same, i.e., $\rho_p \approx \rho_s$. When the ratio of the densities between the phases is relatively large, an additional term $\left[\frac{\rho_p - \rho_s}{2} M(\phi) \nabla (\delta \mathcal{F} / \delta \phi) \cdot \nabla \right] \mathbf{u}$ has to be added at the left hand side, as demonstrated by Albel et al.^[49]

Equation (4) is coupled with Equation (6) and is called as the Cahn–Hilliard–Navier–Stokes model or phase-field model, which is the state-of-the-art method to simulate phase separation involving diffusion and convection in polymer solutions. An important feature of the Cahn–Hilliard–Navier–Stokes model is that it is consistent with the second law of thermodynamics in the sense that $dE_v(\phi, \mathbf{u})/dt \leq 0$. Here, $E_v(\phi, \mathbf{u})$ is the sum of the free energy and the kinetic energy as^[49,59]

$$E_v(\phi, \mathbf{u}) = \int_V [f(\phi) + \kappa (\nabla \phi)^2] dV + \int_V \rho \frac{|\mathbf{u}|^2}{2} dV \quad (7)$$

Herein, we focus only on Newtonian fluids. For readers who are interested in non-Newtonian fluids, such as viscoelastic effect in polymer solutions, we refer to the work of Tanaka.^[33]

3. Diffusion and Hydrodynamics

Diffusion normally prompts the motion of species from a high concentration (chemical potential) to a low concentration (chemical potential) region, resulting in the formation of a uniform system. Contrary to this, inside the spinodal region, the mass transfer is reversed, originating from a negative diffusivity. This abnormal diffusion reduces the free energy functional of the system and is consistent with the second law of thermodynamics. The abnormal diffusion leads to the formation of either a bicontinuous or a droplet-structure (Figure 2c), depending on the initial concentration. When both phases reach their equilibrium concentrations, diffusion still exists between distinct droplets or ligaments because of the inhomogeneous chemical potential induced by the difference in the curvature, which is known as Ostwald ripening. It is noted that in the Ostwald ripening process, the characteristic time for neighboring droplets with a distance L to exchange molecules via the surrounding matrix is $\tau_d = L^2/D_0$. While the characteristic time for a droplet of radius R to drift over the same distance is $\tau_b = L^2/D_R$. Here, D_0 and D_R are diffusion coefficients inversely proportional to the size of the molecule and the radius of the droplets. At the late stage of spinodal decomposition, the droplet is much larger than the molecules, thus $D_0 \gg D_R$ and $\tau_d \ll \tau_b$. Therefore, the composition correlation between adjacent droplets via molecule diffusion takes place long before the drift and collision. It is this composition correlation that engenders nonuniform concentrations along the surface of the droplets. As the interfacial tension has a dependence on the interfacial concentration, an interfacial-tension gradient is established, driving the motion of the droplets. Since additional kinetic energy that is transformed from the free energy appears in the hydrodynamic case, the energetic state as well as the microstructures both differ from the scenario only with diffusion.

In summation, the diffusion and the hydrodynamic mechanisms compete with each other in the entire phase separation process. Since these two mechanisms have distinct characteristic time scales, the morphological evolution of phase separation is dominated by either one of them at different stages of the phase transformation. In the following, we give an overview of the microstructural evolution from the aspects of diffusion and hydrodynamic effect.

4. Diffusion-Governed Microstructural Evolution

4.1. Asynchronous Equilibrium

Because of the cross-linking reaction in polymer solutions, DP increases with time. With an increase of DP, the spinodal as well as the binodal lines both become highly asymmetrical, as illustrated in Figure 2b. In contrast to symmetric or nearly symmetric miscibility gaps in most metals and ceramics, the highly asymmetrical phase diagram is one noteworthy characteristic of polymer solutions. In this section, we give an overview of a recent work which shows that the highly asymmetrical miscibility gap of

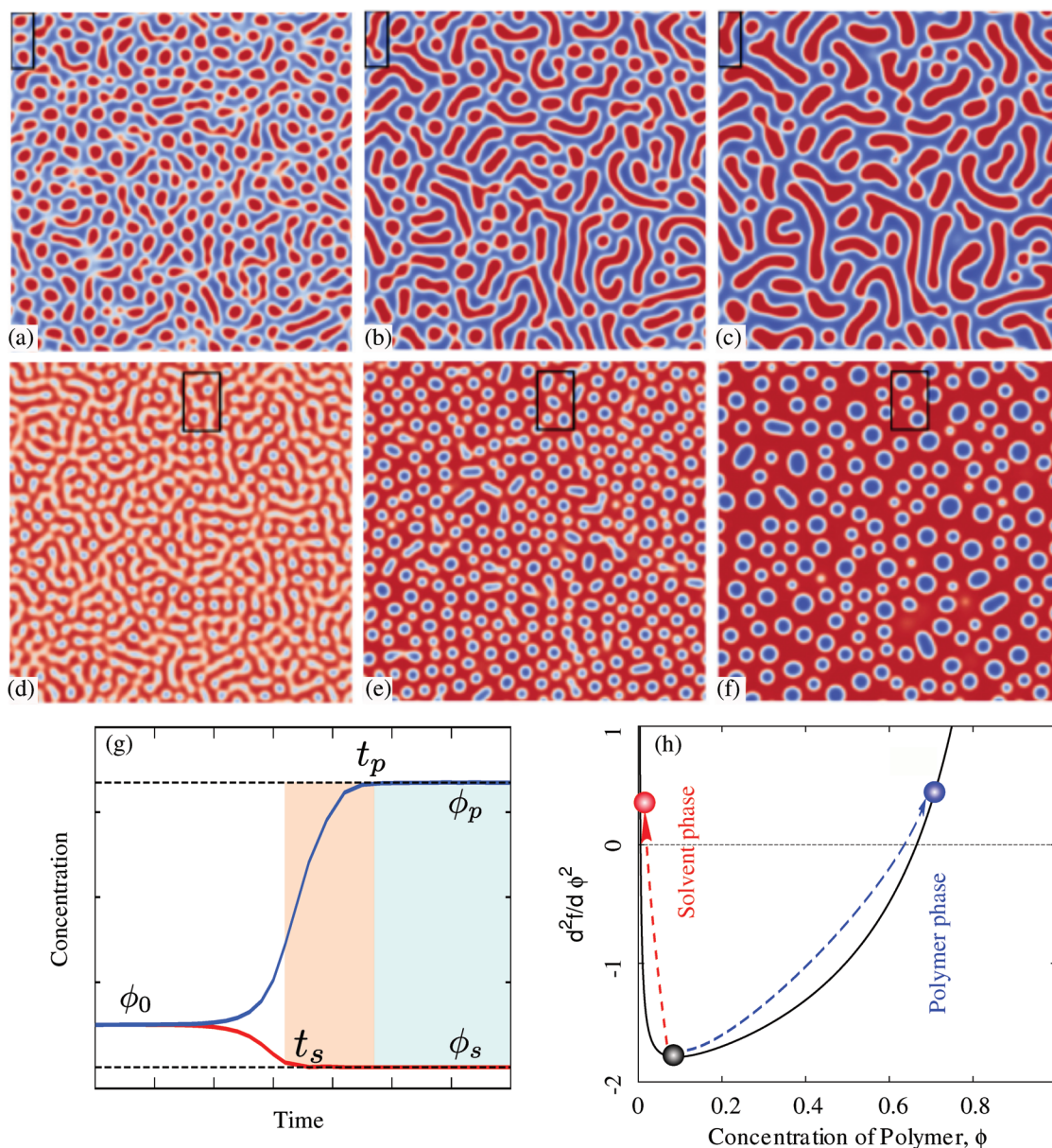


Figure 3. Two morphological transition mechanisms from ref. [60]. Reproduced with permission.^[60] Copyright 2017, American Physical Society. The blue and the red areas represent polymer-rich and solvent-rich phases, respectively. a–c) Transformation from dispersed solvent-droplets into a solvent-cluster, known as “cluster-to-percolation.” d–f) Transformation from a continuous polymer-cluster into dispersed polymer-droplets, known as “percolation-to-droplets.” g) Sketch of the concentration of the polymer-rich (blue line) and the solvent-rich (red line) phases as a function of time. The light orange region depicts the stage where the solvent-rich phase reaches the equilibrium prior to polymer-rich phase. The light blue area shows the stage where both phases are in equilibrium. h) The asynchronous effect arising from the asymmetric driving force $d^2f/d\phi^2$. The black circle illustrates the composition with a maximal driving force and is closer to the solvent side due to polymerization. The red and blue circles represent the equilibrium concentrations of solvent and polymer, respectively.

polymer solutions gives rise to novel microstructural evolution mechanisms in polymer solutions.

Zhang et al.^[60] simulated the microstructural evolution of phase separation in polymer solutions by using a Cahn–Hilliard model coupling with the Flory–Huggins equation with $N = 100$. They reported two morphological transition mechanisms: one is “cluster-to-percolation” (CTP), as shown in Figure 3a–c, where dispersed solvent-droplets transform into a continuous solvent-cluster. The other one is “percolation-to-droplets” (PTD), as

portrayed in Figure 3d–f, where a continuous polymer-cluster decomposes into dispersed polymer-droplets. In Figure 3a–f, the blue phases represent polymer-rich phases and the red ones stand for solvent-rich phases. These two morphological transitions are ascribable to the asynchronous effect, which is schematically depicted in Figure 3g showing the polymer concentration versus time. A polymer solution with an initial concentration ϕ_0 inside the spinodal region decomposes into two phases with equilibrium concentrations ϕ_p (polymer-rich)

and ϕ_s (solvent-rich). The new finding is that there is an intermediate stage ($t_s < t < t_p$) where the solvent-rich phase (red line) has reached the equilibrium, but the polymer-rich phase (blue line) is still far from the equilibrium. This asynchronous effect is due to the high asymmetry of the phase diagram. The detailed interpretation is illustrated in Figure 3h showing the second derivative of the free energy density versus the polymer concentration for $N = 100$. Spinodal decomposition takes place when $d^2f/d\phi^2 < 0$. Zhang et al.^[60] and many other researchers^[33,42] assume an equal diffusivity for polymer and solvent. Thus, in their assumptions, the decomposition rate solely depends upon the absolute value of $d^2f/d\phi^2$. Because of polymerization, the concentration with maximal decomposition rate (black circle) is more close to the solvent phase, so that the solvent phase (orange circle) takes less time to reach the equilibrium than the polymer phase (blue circle). Ipso facto, the diffusivity of long chain polymers in most cases is much less than monomeric solvents. Thus, the asynchronous effect is expected to be more pronounced while considering the difference in the diffusivity of polymers and solvents.

In Figure 3a, because of the asynchronous effect, the polymer species in the gap between two adjacent solvent-droplets has to be rejected into the area outside the gap, leading to a secondary phase separation in the gap. Ascribable to this secondary phase separation, the polymer-rich phase (blue) between two neighboring solvent-droplets gradually transforms into the solvent-rich phase (red). This kind of evolution continues until the two droplets get in touch with each other and reach the equilibrium concentration ϕ_s , giving rise to a “cluster-to-percolation” transition. This transition has been captured in experiments.^[61] The interpretation of the PTD transition is analogous to CTP. A Gaussian distributed noise produces a structure with 50% polymer-rich phases and 50% solvent-rich phases, which is fair for both phases. This structure consists of continuous polymer-clusters, as depicted in Figure 3d. At this stage, the solvent-matrix has already reached the equilibrium, but the polymer-cluster is still on the way to arrive at the equilibrium. This asynchronous effect causes a secondary phase separation in the polymer-clusters, resulting in the PTD transition (Figure 3e). The PTD transition reported by Zhang et al.^[60] is observed at the critical composition and thus differs from the PTD phenomenon at off-critical compositions in systems with symmetric miscibility gaps. After PTD, the concentration in the polymer-droplets has not yet reached the equilibrium value, so that the polymer-droplets continuously grow with time (Figure 3f) until the equilibrium volume fraction is achieved according to the lever rule.

Although the final volume fraction can be predicted by the lever rule for a given initial concentration ϕ_0 , the morphological evolution toward the equilibrium states has not been fully revealed before this work. From this point of view, the work of Zhang et al. has made a great step toward the understanding on the morphological evolution of phase separation in polymer solutions. After the asynchronous stage ($t > t_p$ in Figure 3g) where both phases reach the equilibrium concentrations, the dominant mechanism for the morphological evolution is Ostwald ripening, where big droplets grow at the expense of small droplets. This evolution results in a coarse and inhomogeneous structure, in contrast to the fine and homogeneous structures at

the asynchronous stage. In order to enhance the structural properties, it would be of sense to delay the asynchronous stage by controlling kinetic parameters, such as mobility.

4.2. Mobility

The asynchronous effect is attributed to the asymmetric thermodynamic driving force $-\nabla(\delta\mathcal{F}/\delta\phi)$ from the phase diagram. It is noted that the kinetics is affected not only by the thermodynamic driving force but also by the mobility. There are two kinds of mobility in the literature. The first one is a concentration-independent mobility that is used, for example, by Zhang et al.^[60] to explore the asynchronous effect. Two typical concentration-independent mobilities are Rouse and Zimm models.^[41] In the former case, the mobility is inversely proportional to DP, $M = M_0/N$, with M_0 being a positive constant. This derivation is based on the consideration that a single polymer-chain diffusion is engendered by Brownian motion of beads connected by harmonic springs. The Rouse mobility has been used by Chan^[62] and Yang^[63] to simulate phase separation in polymer solutions. The shortcoming of the Rouse model is ascribed to the neglect of hydrodynamic interactions. By including hydrodynamic interactions between beads with the Kirkwood–Riseman approximation, the Rouse model is improved as^[41]

$$M = M_0/N^\nu \quad (8)$$

which is the Zimm model and ν is a Flory exponent. The Zimm mobility reduces to the Rouse model when $\nu = 1$ and is consistent with the experimental data for dilute polymer solutions. Both the Rouse and Zimm mobilities are time-dependent. These two models are just interested in the mobility of one single polymer strand in a solution. They do not take into account effects of the surrounding solvent and thus is well appropriate for dilute polymer solutions. The concentration-independent mobility simplifies the complex transport equations in polymer solutions and is able to mimic some fluid dynamic phenomena without solving the hydrodynamic equations (see ref. [64]).

The second type of the mobility depends on the driving force of the phase separation as $M = D/\partial^2f/\partial\phi^2$, where D is the manual diffusion coefficient. This equation is derived by comparing the diffusion flux expressed in terms of the chemical potential $\mathbf{J} = -M\nabla\mu$ to the Fick's flux $\mathbf{J} = -D\nabla\phi$. This consideration yields a concentration-dependent mobility. A common used concentration-dependent mobility is^[62]

$$M = D\phi(1-\phi)/(k_bT) \quad (9)$$

for a binary system, which is based on the ideal solution free energy model $f(\phi) = k_bT[\phi\ln\phi + (1-\phi)\ln(1-\phi)]$ with $\partial^2f/\partial\phi^2 = \phi(1-\phi)/k_bT$. It is evident that the ideal solution free energy model cannot give rise to phase separation since the second derivative of the free energy density with respect to the concentration is always positive. By using the Flory–Huggins free energy model rather than the ideal solution model, a more generalized mobility

$$M = D/k_bT[1/(N\phi) + 1/(1-\phi) - 2\chi] \quad (10)$$

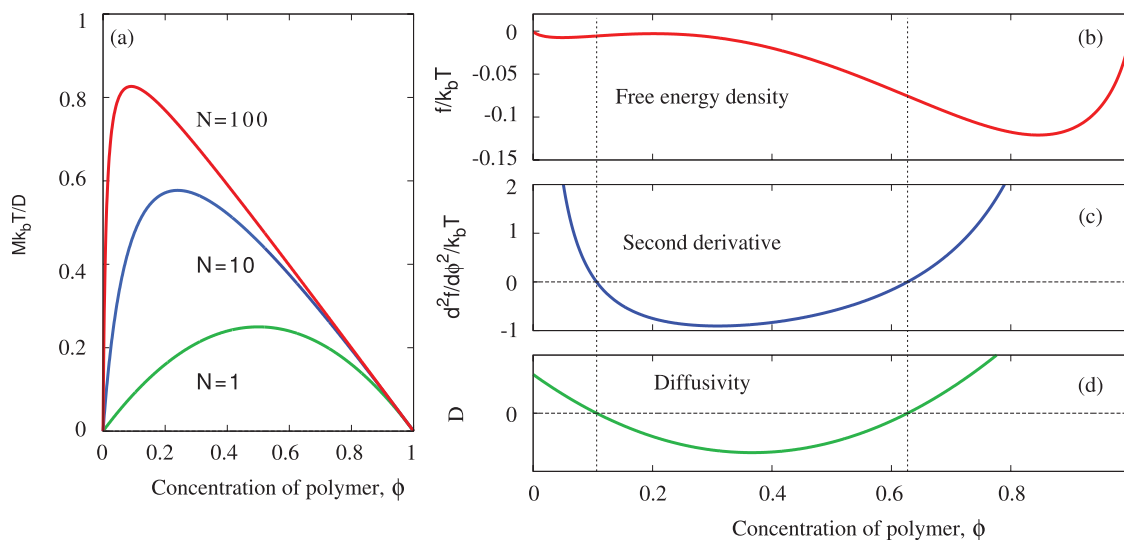


Figure 4. Interpretation of the mobilities used in the literature: a) The dimensionless mobility $Mk_b T/D$ as a function of the polymer concentration ϕ for $\chi = 0$. The violet line shows the mobility of Equation (9) used in ref. [62]. The green and the blue lines illustrate the mobility of Equation (10) used in refs. [48,66] with $N = 10$ and $N = 100$, respectively. b) The free energy density and c) the corresponding second derivative according to the Flory–Huggins theory with $N = 5$. d) A sketch for the diffusivity varying with the polymer concentration.

is obtained. Equation (10) is a recent important progress for simulating phase separation in polymer solutions.^[48] The significance of this mobility is that it is asymmetrical when $N > 1$ and the extent of the asymmetry increases with N , as depicted in Figure 4a. Since the new mobility shifts toward the solvent side for large DPs, a direct consequence is that the solvent-rich phase reaches the equilibrium even earlier than the polymer-rich phase. Thus, the free energy density dependent mobility is expected to increase the asynchronous time interval, which could be an interesting point in a future study.

Although the utilization of a generalized mobility is a remarkable step, there are still some issues open for discussion. A fact is that the second derivative of the free energy density, which is the denominator in Equation (10), is negative inside the spinodal region and positive outside the spinodal region. Therefore, we have a constraint for the sign of the diffusivity that depending upon the sign of $\partial^2 f/\partial\phi^2$ to ensure $M > 0$, as pointed by Janssens et al.^[65] In most studies, the diffusivity D is assumed to be a positive constant, which apparently does not fulfill this constraint. Even a concentration-dependent mobility $D(\phi)$ is used in few cases,^[48] the sign of the diffusivity remains positive. Another issue is that if we postulate that the diffusivity is continuous and differentiable, the diffusion coefficient would be zero at the spinodal points. As a result, a “0/0”-type mobility occurs at the spinodal points. The scenario elucidated here is sketched in Figure 4b–d. According to the foregoing discussions, the diffusivity should be a nonlinear function depending on the concentration ϕ . The asymmetry of the mobility is affected by the nonlinear relation $D(\phi)$.

5. Hydrodynamic Effects

Phase separation in polymer solutions is a very complex physical phenomenon involving not only diffusion but also fluid

flow. In this section, we give an overview of a novel microstructural evolution mechanism from Shimizu and Tanaka^[42] by considering hydrodynamic effects. We shall see that the motion of the droplets during phase separation follows a deterministic rather than a stochastic nature. The deterministic mechanism revealed by Shimizu and Tanaka is on the basis of a solutal Marangoni force induced by inhomogeneous interfacial concentrations. This mechanism significantly changes the understandings on the microstructural evolution of phase separation.

Figure 5a sketches two different sized droplets from phase separation. Let us assume that the droplets and the matrix both have reached the equilibrium states. According to the Ostwald mechanism, the big droplet always grows at the expense of the small droplets due to the difference in the curvature. The growing flux is represented by the black arrows, perceptually from the small to the big droplets. The concentration gradient in the gap between the two droplets is higher than the one outside the gap because of distinct lengths of the diffusion paths. If the diffusivity is isotropic, the magnitude of the diffusion flux in the gap is greater than that outside the gap. As a result, the difference in the diffusion fluxes gives rise to a concentration gradient around the surface of each droplets, as sketched by the blue dashed lines. In most cases, the surface tension increases with the concentration, so that the surface tension adjacent to the gap is less than other positions. The established surface tension or concentration gradients consequently prompt the motion of the droplet arising from the hydrodynamic force, $-\nabla_s \sigma$ or $-\nabla_s \phi$.

In a system consisting of multidroplets as in Figure 5b–e, which are typical phase separation microstructures at off-critical compositions, the motion of the resulting droplets seems to be stochastic, governed by the Brownian motion mechanism, also known as Binder–Stauffer–Siggia mechanism. In this case, the trajectories of the mass-center of two adjacent droplets are

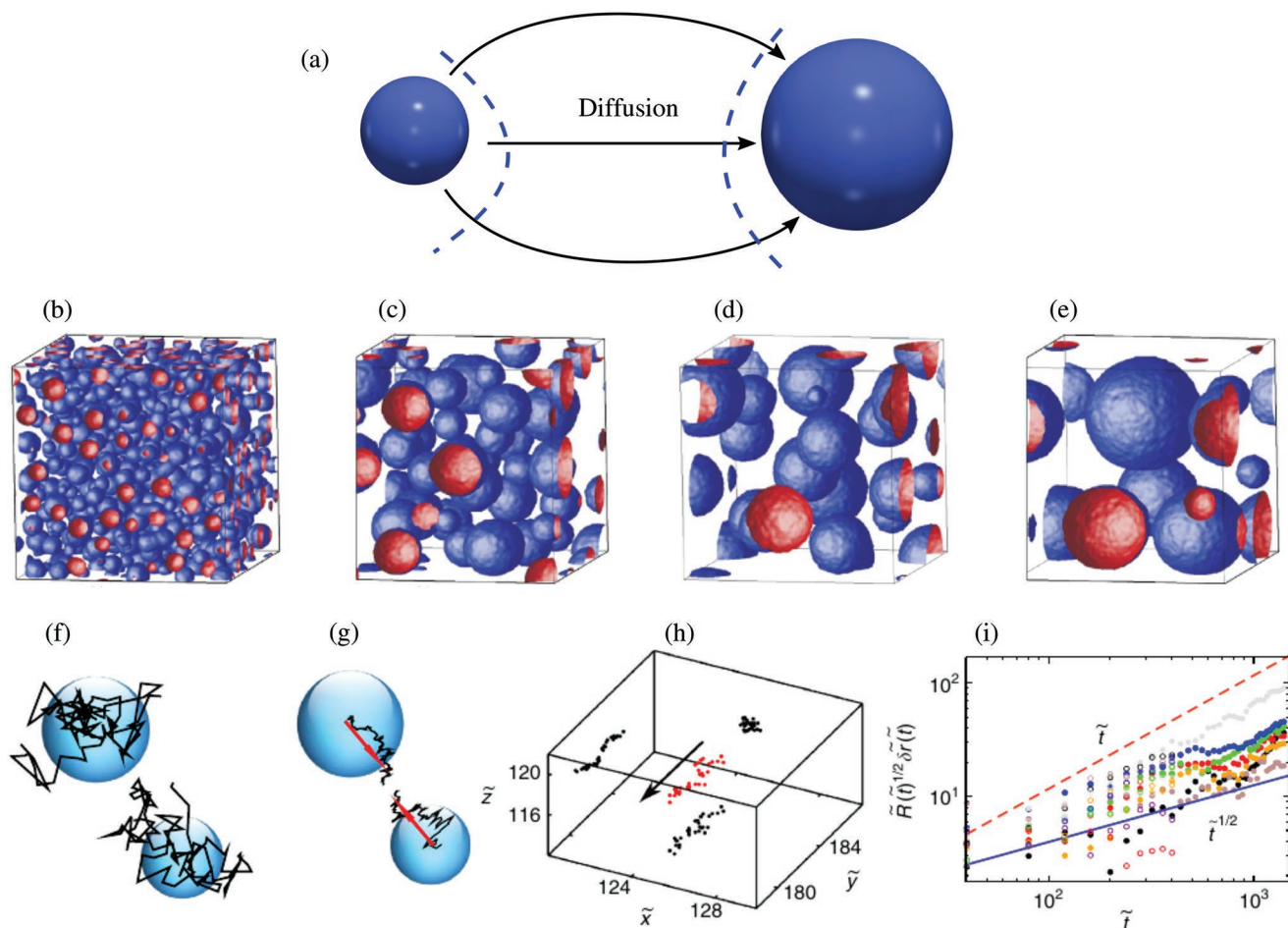


Figure 5. Spontaneous motion of droplets. a) Sketch for the concentration gradient due to different diffusion paths. b–e) Phase separation microstructures at different times with an initial concentration $\phi_0 = 0.25$. f,g) Schematic pictures for random and directional motions, respectively. h) An example of the temporal evolution of the barycenter of a single droplet from the microstructures shown in (b)–(e). i) Symbols with different colors depict the dimensionless displacements of different droplets shown in (b)–(e) as a function of time. The blue straight line illustrates the displacement from Brownian motion and the red dashed line has a slope of 1 corresponding to Marangoni effect. b–i) Reproduced with permission.^[42] Copyright 2015, Springer Nature.

random as illustrated in Figure 5f. However, as demonstrated by Shimizu and Tanaka, the motion of the droplets resulting from phase separation does not follow the stochastic behavior of Brownian motion. Instead, the movement of the droplets is directional, as sketched by the red line in Figure 5g. A clear evidence is shown in Figure 5h, where the mass-center of a single droplet in the microstructures from phase separation shifts toward a particular direction with time. This directional moving behavior is further confirmed by analyzing the displacements of different droplets with time in Figure 5i. For the Brownian motion governed movement, the mean-square displacement δr follows the $t^{1/2}$ -relation as $\delta r = \sqrt{k_B T / (5\pi\eta R)} \sqrt{\tilde{t}}$ (the blue solid line). However, the displacements of different droplets before collision during the phase separation, which are represented by different colored symbols, are much greater than the ones of the Brownian motion mechanism and almost obey a linear law $\delta r \sim t$ (the red dashed line), which is a characteristic of hydrodynamic effect. This observation contradicts to the behavior of the conventional stochastic motion.

A more heedful scrutiny on Figure 5i shows that the displacements of the droplets lay in between the Brownian motion line and the Marangoni line. This is a strong evidence that the Marangoni effect is as crucial as the Brownian motion in a multidroplets system. Moreover, we notice that in Figure 5i, there are few displacements (open red and filled black circles) below the Brownian motion line. These displacements correspond to tiny droplets shrinking with time due to Oswald ripening. The physical picture for those tiny droplets is that the molecular diffusion transport is much faster than the Brownian motion as well as the Marangoni effect. In other words, the characteristic time for the molecular diffusion τ_d is much less than the ones of the Brownian motion τ_b and the fluid flow $\tau_v = \eta R / \sigma$. The importance of directional movements of droplets due to Marangoni force in a multidroplets system has also been realized in diffusiophoresis and diffusioosmosis.^[67]

The nonstochastic behavior reported by Shimizu and Tanaka^[42] indicates a new type of droplet motion from a stochastic to deterministic nature. This deterministic phenomenon

has also been studied in refs. [68,69]. In the deterministic scenario where the hydrodynamic effect is more significant than diffusion, the small droplets swim faster than the large ones,^[68] which eventually leads to an intercollision that large droplets eat neighboring small droplets, similar to the classic Lifshitz, Slyozov, Wagner (LSW)^[70,71] scenario. We stress that this deterministic hydrodynamic effect is only significant when the droplets have a strong interaction with each other, which occurs if the initial concentration is relatively high. When the initial concentration is low, i.e., dilute solution, the volume fraction of the droplets is fairly small, so that the interaction between the droplets is weak and the hydrodynamic effect is irrelevant. In dilute solutions, diffusion is more important than the hydrodynamic transport and the microstructural evolution follows the LSW theory.

Shimizu and Tanaka explored this deterministic nature for systems with a perfectly symmetric miscibility gap. So far, the state-of-the-art investigation has seldomly considered this deterministic nature for the phase separation in polymer solutions

with a highly asymmetric phase diagram. As mentioned above, the polymer-rich and the solvent-rich phases asynchronously arrive at the equilibrium states when phase diagram is not symmetric. In the asynchronous stage, there are three mechanisms for the microstructural evolution: i) a second phase separation in the nonequilibrium polymer-rich phase, ii) the Ostwald mechanism where big polymer-droplets eat small ones, and iii) directional movement of polymer-droplets because of the nonuniform concentration around the surface of the droplets induced by the droplet-interaction. If the hydrodynamic effect is dominant over diffusion, the droplets may move fast enough such that the second phase separation between two adjacent droplets is completely suppressed.

A recent important progress is an extension of this deterministic nature to a ternary polymer–solvent–nonsolvent system, as done by Tree et al.^[43] The difference is that a flat interface is considered here rather than spheres. Their main results are shown in **Figure 6a–d**. Initially, a phase composed of polymer, solvent and nonsolvent is placed on top of another phase mostly

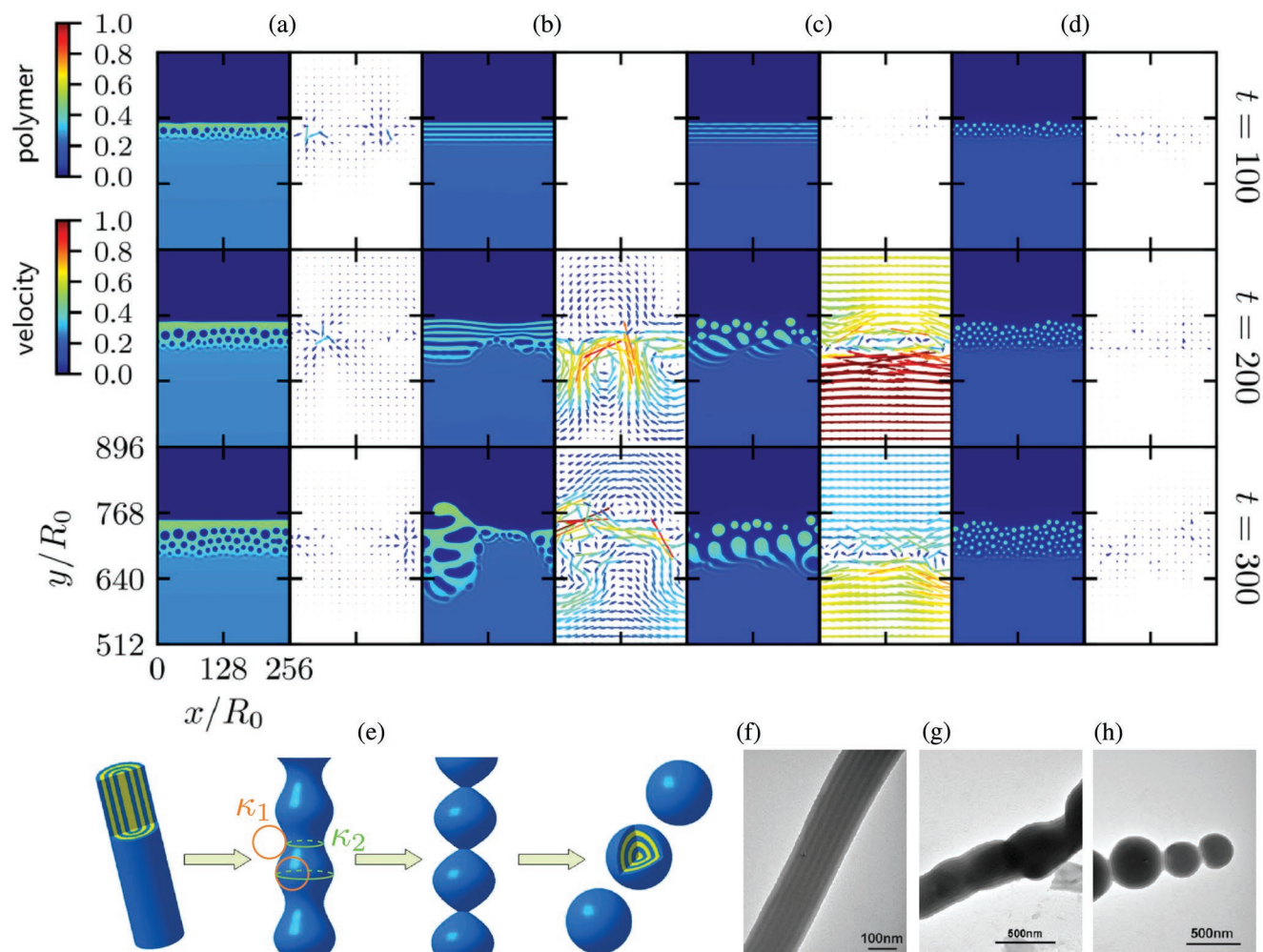


Figure 6. Hydrodynamic instability in polymer structures. a–d) The Sternling and Scriven instability during phase separation in a ternary polymer solutions shown by Tree et al.^[43] Reproduced with permission.^[43] Copyright 2018, American Chemical Society. e–h) Plateau–Rayleigh instability for a polymer nanorod. Reproduced with permission.^[73] Copyright 2015, American Chemical Society. The interpretation for the curvatures κ_1 and κ_2 in (e) is from the present authors.

containing the nonsolvent species. The concentrations in these two phases are not in equilibrium, so that the polymer species is transported across the interface via diffusion. The diffusion from one phase to another phase provokes a surface-directed spinodal decomposition, which produces droplet-structures at off-critical compositions (Figure 6a,d) and lamellar-structures nearby the critical compositions (Figure 6b,c). However, the mass flux is governed not only by diffusion but also convection. Because of the difference in the ratio of diffusivity to viscosity in these two phases, polymer-rich and polymer-lean regions appear at the interface due to a competition effect between diffusion and convection. This inhomogeneous concentration along/near the interface leads to a surface tension gradient, yielding a hydrodynamic force $-\nabla_s \sigma$ or $-\nabla_s \phi$, as in the case of Shimizu and Tanaka. The hydrodynamic force further gives rise to a hydrodynamic instability, which is known as Sternling and Scriven instability.^[72] This instability leads to the breakup of the lamellar structure of spinodal decomposition, as depicted in Figure 6b,c). This is a first work to simulate the Sternling and Scriven instability in a ternary polymer system. Contrasting to most previous simulations which only consider the diffusion mechanism, the work of Tree et al. demonstrates that the deterministic hydrodynamic effect can result in different microstructures of phase separation. For instance, a bicontinuous or lamellar phase separation structure is formed at the critical composition only with diffusion. But the hydrodynamic instability can engender a transformation from the bicontinuous structure into dispersed droplets.

It should be noted that the Sternling and Scriven instability is applied to a 2D semi-infinite system, where the mean curvature is zero. An important contribution from the mean curvature to the microstructural evolution in polymer solutions is shown in a recent work of Yan et al.^[73] In this work, it is found that a polystyrene-*block*-poly(4-vinylpyridine) (PS-*b*-P4VP) nanorod decomposes into several polymer-particles. The morphological transition is sketched in Figure 6e and the corresponding experimental results are illustrated in Figure 6f–h. This morphological transition is well-known as the Plateau–Rayleigh instability. The mechanism behind this transition is that the mean curvature has two contributions in three dimensions, namely, $\kappa = \kappa_1 + \kappa_2$, where κ_1 is the two dimensional curvature, the radius of which is shown by the orange circle in Figure 6e. In two dimensions, the mean curvature is positive at the crest and negative at the trough, so that the diffusion or hydrodynamic fluxes are always from the crest to the trough, smoothing out the roughness at the interface. The other curvature κ_2 is the contribution from the third dimension and the radius is schematically depicted by the green circles. The third dimensional curvature at the trough is greater than the one at the crest. Thus, the total curvature at the trough could be greater than the one at crest, which results in a diffusion or hydrodynamic flux from the trough to the crest, provoking an amplification of the roughness, which is another hydrodynamic instability. In the study of Shimizu and Tanaka, the particles have uniform curvatures. The simulations of Tree et al. are performed in two dimensions. Hence, this hydrodynamic effect originating from curvature has not been shed light on in both works. It would be insightful to consider both deterministic natures: curvature as well as interfacial-tension-gradient in future studies.

6. Structure Characterization

As phase separation processes result in porous microstructures in which a certain degree of randomness, e.g., pore size distributions, is unavoidable, statistical characterization concepts get increasingly attractive.^[74–77] The statistical characterization is based on functions which essentially capture the spatial correlation among different locations in the microstructure. Since microstructures of phase separation show different natures, e.g., bicontinuous clusters and dispersed droplets, a variety of statistical functions exist.^[76] For instance, two-point correlation functions provide a very comprehensive picture of the salient features of bicontinuous microstructures, but generally creates an extremely large feature space as well. In order to reduce the dimensionality of the data, a principal component analysis (PCA)^[78–81] is performed on the two-point statistics. By PCA the data is represented on a transformed coordinate system where the axes are oriented according to the variance in structure properties. Typically, the principal components (PC 1, PC 2, etc.) are ordered from the highest to the lowest variance starting with PC 1. As a main advantage, PCA is capable of emerging the main characteristics in microstructures as well as classifying a huge set of data in an unsupervised manner. That is, no prior information about the characteristics of the data is needed. The features are solely identified by representing the microstructures in low dimensional space.

Some insightful examples are presented in Figure 7 where two-point correlation functions and PCA are applied for porous two-phase systems. Figure 7a shows the classification of two dissimilar porous components of polymer electrolyte fuel cells. Here, PCA classifies the gas diffusion layer (GDL) and microporous layer (MPL) by their distinct intrinsic structure properties. In the PC space, the characterization is expressed by so called point clusters where each point represents a different representative volume element of the microstructures.^[82] In Figure 7b, the resulting two-point correlation function is visualized for three different microstructures. The depicted spatial statistics highlights the evident differences in the three morphologies.^[83] Figure 7c illustrates an example for the feature extraction in X-ray computer tomography scans (X-CT) from a polymeric porous structure. For the characterization, a set of 8424 porous structures with defined features are algorithm-based generated and both the X-CT scans and the generated structures are scrutinized. In low dimensional space, PC 1 and PC 2 are interpreted as porosity and mean pore sizes, respectively, while PC 3 and PC 4 characterize geometrical anisotropies in x -, y -, and z -direction. By searching for point clusters of X-CT and the generated structures, a geometrical anisotropy in z -direction is detected for the investigated PPM.^[84]

7. Conclusion

In conclusion, we have given an overview of several novel evolution mechanisms for the microstructures of phase separation from two different aspects: diffusion and hydrodynamics. In the case of diffusion-governed evolution, the polymer-rich phase always reaches the equilibrium state later than the

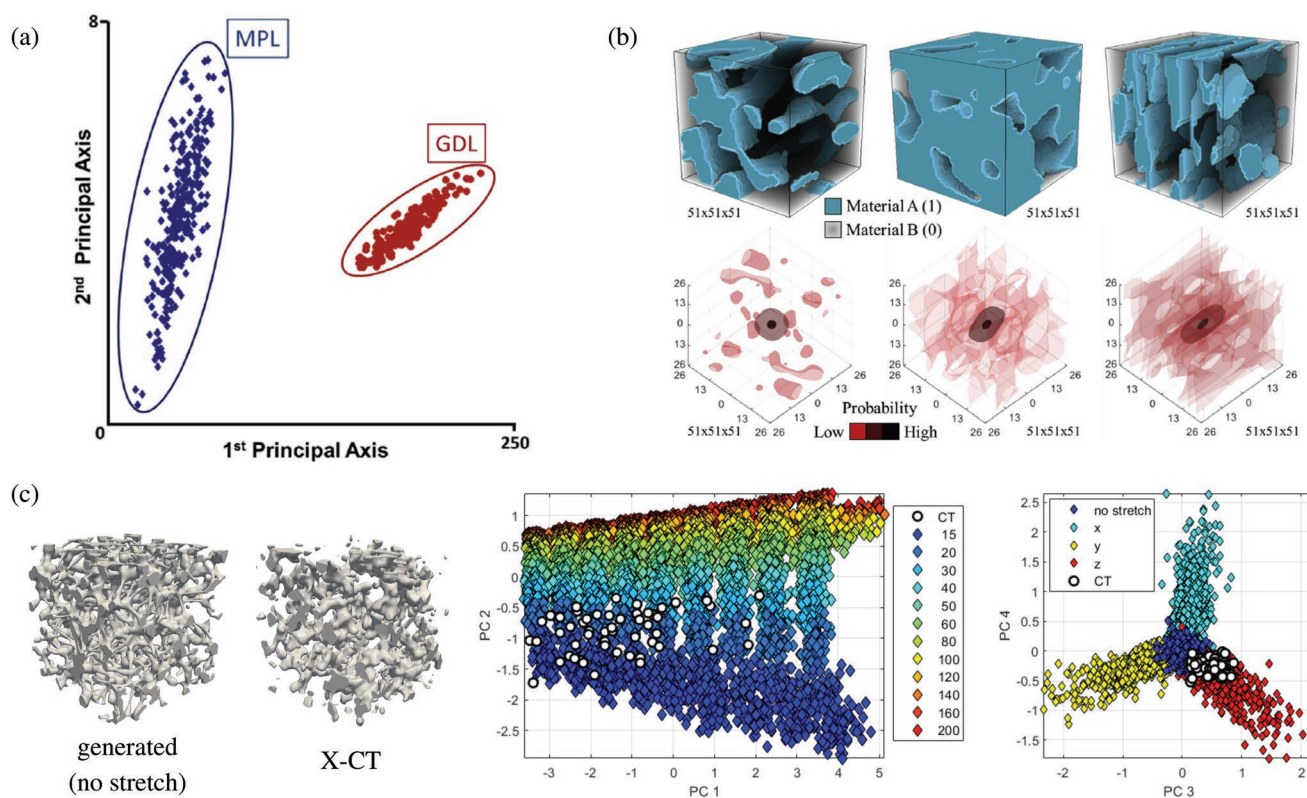


Figure 7. Selected examples from literature where two-point correlation functions and principal component analysis are used for characterization and classification of porous microstructures. a) Classification of porous components (GDL, MPL) in a polymer electrolyte fuel cell by their structural properties in the principal component space (PC 1 and PC 2). Reproduced with permission.^[82] Copyright 2014, Elsevier. b) Visualization of the two-point correlations for three different microstructures. Reproduced with permission.^[83] Copyright 2018, Elsevier. c) Feature extraction of X-ray computer tomography scans of PPM by generating algorithm-based 8424 porous structures with defined properties and investigating the variances in the PC space. PC 1 and PC 2 are interpreted as the porosity and the mean pore (bottom middle), respectively, while in PC 3 and PC 4, geometrical anisotropies (stretched structures) in x -, y -, and z -direction are found (bottom right). Reproduced with permission.^[84] Copyright 2017, Elsevier.

solvent-rich phase because of the asymmetrical thermodynamic driving force. This asynchronous effect results in two novel morphological transitions: “cluster-to-percolation” and “percolation-to-droplets.” This finding is a great step toward understandings on the microstructural evolution of phase separation in polymer solutions. The asynchronous effect is affected not only by the thermodynamic driving force but also by the mobility, which is assumed to be a constant value in the work of Zhang et al.^[60] As reviewed, the mobility in general depends on the thermodynamic driving force and becomes high asymmetric for large DPs. Thus, the asynchronous effect is expected to be more pronounced when using an asymmetric mobility.

A second focus herein is the microstructural evolution of phase separation dedicated by hydrodynamics. One noteworthy finding is that the droplets resulting from phase separation exhibit a directional moving behavior, contrary to the conventionally stochastic movement of Brownian motion. This directional movement is essentially caused by an interface-tension-gradient which is induced by the composition correlation between neighboring droplets. The interface-tension-gradient can also be achieved through a competition effect between diffusion and convection, which could produce a hydrodynamic instability during phase separation. This hydrodynamic

instability is a new freedom to affect the microstructural evolution of phase separation in polymer solutions.

In a pure diffusion case, the mean radius of the droplets follows the LSW theory^[70] as $\langle R(t) \rangle \sim t^{1/3}$. However, this quintessential theory is only applicable when the matrix and the droplets are at rest. When the droplets exhibit directional center-to-center movement induced by Marangoni force, the mean radius obeys another power law^[85] $\langle R(t) \rangle \sim t^{1/2}$. These different mechanisms of microstructural evolution have respective characteristic time scales related to the size of the droplets. Thus, the microstructural evolution and the mean pore size of PPM from phase separation shall be contemplated distinguished from the time stage associated with different underlying mechanisms.

It is noteworthy that the asynchronous effect is intrinsically caused by the diffusion mechanism. As Marangoni flow influences the spatial arrangement of droplets, the diffusion routes between droplets are consequently altered. Therefore, this asynchronicity is indirectly affected by the Marangoni convection. It remains an open question to elaborate the coupling effects of these two mechanisms. Moreover, each mechanism has its individual time scale. It is insightful to shed light on a better understanding about the dominant mechanism at different stages of phase separation. Furthermore, diffusion normally

generates a bicontinuous PPM at the critical composition. Combining with Marangoni flow, the bicontinuous PPM show more variations in morphologies, such as magnum droplets, tiny dispersion or clusters.

Last but not least, an overview of the recent progress in a novel characterization technique, namely, PCA, used to porous structures is given. In contrast to other conventional characterization methods, PCA is capable of analyzing the spatial statistics of porous structures. This capability can be applied to achieve a deep insight into the underlying mechanisms of phase separation, for instance, scrutinizing the correlation between droplets in the deterministic nature of droplet-motion and revealing unknown morphological characteristics, such as anisotropy, in the asynchronous stage.

Acknowledgements

F.W. and P.A. contributed equally to this work. The authors thank for support through the coordinated research programme “Virtual Materials Design (VirtMat)” funded by the Helmholtz association. Furthermore, the authors acknowledge support of the German Research Foundation (DFG) for enabling further research in developing new models for polymerization through the Gottfried-Wilhelm Leibniz programme NE 822/31 and through the initiative “NanoMembrane” within the research programme “Science and Technology of Nanosystems (STN).”

Conflict of Interest

The authors declare no conflict of interest.

Keywords

capillarity, principal component analysis (PCA), phase-field, phase separation, polymer solutions

Received: October 17, 2018
Revised: November 22, 2018
Published online: March 11, 2019

- [1] D. Wu, F. Xu, B. Sun, R. Fu, H. He, K. Matyjaszewski, *Chem. Rev.* **2012**, *112*, 3959.
- [2] M. Ulbricht, *Polymer* **2006**, *47*, 2217.
- [3] M. Stucki, M. Loepfe, W. J. Stark, *Adv. Eng. Mater.* **2018**, *20*, 1700611.
- [4] S. D. Kimmins, N. R. Cameron, *Adv. Funct. Mater.* **2011**, *21*, 211.
- [5] S. Andrieux, A. Quell, C. Stubenrauch, W. Drenckhan, *Adv. Colloid Interface Sci.* **2018**, *256*, 276.
- [6] A. Kelly, *Philos. Trans. R. Soc., A* **2006**, *364*, 5.
- [7] X. Zou, G. Zhu, *Adv. Mater.* **2018**, *30*, 1700750.
- [8] N. A. Marrufo-Hernández, M. Hernández-Guerrero, J. M. Nápoles-Duarte, J. P. Palomares-Báez, M. A. Chávez-Rojo, *AIP Adv.* **2018**, *8*, 035308.
- [9] W. A. Phillip, B. O'Neill, M. Rodwogin, M. A. Hillmyer, E. Cussler, *ACS Appl. Mater. Interfaces* **2010**, *2*, 847.
- [10] A. Lee, J. W. Elam, S. B. Darling, *Environ. Sci.: Water Res. Technol.* **2016**, *2*, 17.
- [11] T. Kulkarni, G. Slaughter, *Membranes* **2016**, *6*, 55.
- [12] B. J. Lambert, F. W. Tang, W. J. Rogers, *Polymers in Medical Applications*, Smithers Rapra Publishing, Shawbury, Shrewsbury, UK **2001**.
- [13] D. Gasperino, T. Baughman, H. V. Hsieh, D. Bell, B. H. Weigl, *Annu. Rev. Anal. Chem.* **2018**, *11*, 219.
- [14] I. Pulko, J. Wall, P. Krajnc, N. R. Cameron, *Chem. Eur. J.* **2010**, *16*, 2350.
- [15] M. Rose, *ChemCatChem* **2014**, *6*, 1166.
- [16] D. Guy, B. Lestriez, D. Guyomard, *Adv. Mater.* **2004**, *16*, 553.
- [17] D. Mukherjee, G. Y. K. Guruprasada, H. M. Nimbegondi Kotresh, S. Sampath, *ACS Appl. Mater. Interfaces* **2016**, *9*, 19446.
- [18] J. H. Zeng, Y. F. Wang, S. Q. Gou, L. P. Zhang, Y. Chen, J. X. Jiang, F. Shi, *ACS Appl. Mater. Interfaces* **2017**, *9*, 34783.
- [19] L. Nyholm, G. Nyström, A. Mhryan, M. Strømme, *Adv. Mater.* **2011**, *23*, 3751.
- [20] T. Yamaguchi, F. Miyata, S. I. Nakao, *Adv. Mater.* **2003**, *15*, 1198.
- [21] Y. Zhang, S. Zha, M. Liu, *Adv. Mater.* **2005**, *17*, 487.
- [22] J. Huang, C. A. Tao, Q. An, W. Zhang, Y. Wu, X. Li, D. Shen, G. Li, *Chem. Commun.* **2010**, *46*, 967.
- [23] F. García-Santamaría, M. Xu, V. Lousse, S. Fan, P. V. Braun, J. A. Lewis, *Adv. Mater.* **2007**, *19*, 1567.
- [24] T. J. Peckham, S. Holdcroft, *Adv. Mater.* **2010**, *22*, 4667.
- [25] P. Sun, K. Wang, H. Zhu, *Adv. Mater.* **2016**, *28*, 2287.
- [26] R. D. Bennett, A. J. Hart, R. E. Cohen, *Adv. Mater.* **2006**, *18*, 2274.
- [27] W. Joo, H. J. Kim, J. K. Kim, *Langmuir* **2010**, *26*, 5110.
- [28] N. Zhou, F. S. Bates, T. P. Lodge, *Nano Lett.* **2006**, *6*, 2354.
- [29] B. Wolf, R. Scirocco, W. Frith, I. Norton, *Food Hydrocolloids* **2000**, *14*, 217.
- [30] V. Gopishetty, I. Tokarev, S. Minko, *J. Mater. Chem.* **2012**, *22*, 19482.
- [31] A. Hara, R. Inoue, N. Takahashi, K. Nishida, T. Kanaya, *Macromolecules* **2014**, *47*, 4453.
- [32] C. Schugens, V. Maquet, C. Grandfils, R. Jérôme, P. Teyssie, *J. Biomed. Mater. Res.* **1996**, *30*, 449.
- [33] H. Tanaka, T. Araki, *Chem. Eng. Sci.* **2006**, *61*, 2108.
- [34] T. Domenech, S. S. Velankar, *J. Rheol.* **2017**, *61*, 363.
- [35] Q. Yang, K. Loos, *Polymers* **2017**, *9*, 525.
- [36] X. Rui, Z. Song, S. Jing, T. Decheng, *Polym. J.* **2005**, *37*, 560.
- [37] Z. Luo, Y. Li, B. Liu, *Chem. Commun.* **2017**, *53*, 8649.
- [38] N. Zhao, Q. Xie, L. Weng, S. Wang, X. Zhang, J. Xu, *Macromolecules* **2005**, *38*, 8996.
- [39] M. C. Chang, *J. Korean Ceram. Soc.* **2016**, *53*, 50.
- [40] P. J. Flory, *J. Chem. Phys.* **1942**, *10*, 51.
- [41] A. A. Teraoka, I. Teraoka, *Polymer Solutions: An Introduction to Physical Properties*, John Wiley & Sons, New York **2002**.
- [42] R. Shimizu, H. Tanaka, *Nat. Commun.* **2015**, *6*, 7407.
- [43] D. R. Tree, T. Iwama, K. T. Delaney, J. Lee, G. H. Fredrickson, *ACS Macro Lett.* **2018**, *7*, 582.
- [44] J. Zhu, X. Lu, R. Balieu, N. Kringos, *Mater. Des.* **2016**, *107*, 322.
- [45] W. H. Carothers, *Chem. Rev.* **1931**, *8*, 353.
- [46] P. J. Flory, *Principles of Polymer Chemistry*, Cornell University Press, London, UK **1953**.
- [47] J. W. Cahn, J. E. Hilliard, *J. Chem. Phys.* **1958**, *28*, 258.
- [48] Y. Mino, T. Ishigami, Y. Kagawa, H. Matsuyama, *J. Membr. Sci.* **2015**, *483*, 104.
- [49] H. Abels, H. Garcke, G. Grün, *Math. Models Methods Appl. Sci.* **2012**, *22*, 1150013.
- [50] F. Wang, A. Choudhury, M. Selzer, R. Mukherjee, B. Nestler, *Phys. Rev. E* **2012**, *86*, 066318.
- [51] A. Naso, L. Ó. Náraigh, *Eur. J. Mech. B/Fluids* **2018**, *72*, 576.
- [52] X. Yang, *J. Sci. Comput.* **2018**, *74*, 1533.
- [53] Y. Cai, J. Shen, *Math. Comput.* **2018**, *87*, 2057.
- [54] Z. Guo, P. Lin, J. Lowengrub, S. M. Wise, *Comput. Methods Appl. Mech. Eng.* **2017**, *326*, 144.
- [55] D. Jacqmin, *J. Comput. Phys.* **1999**, *55*, 96.

- [56] B. Nestler, A. A. Wheeler, L. Ratke, C. Stöcker, *Physica D* **2000**, *141*, 133.
- [57] D. M. Anderson, G. B. McFadden, A. A. Wheeler, *Physica D* **2000**, *135*, 175.
- [58] J. Kim, *Commun. Comput. Phys.* **2012**, *12*, 613.
- [59] J. Zhao, Q. Wang, X. Yang, *Comput. Methods Appl. Mech. Eng.* **2016**, *310*, 77.
- [60] G. Zhang, T. Yang, S. Yang, Y. Wang, *Phys. Rev. E* **2017**, *96*, 032501.
- [61] M. Okada, K. Fujimoto, T. Nose, *Macromolecules* **1995**, *28*, 1795.
- [62] P. K. Chan, *Model. Simul. Mater. Sci. Eng.* **2006**, *14*, 41.
- [63] J. Yang, R. Bai, Z. Suo, *Adv. Mater.* **2018**, *30*, 1800671.
- [64] K. Kamata, T. Araki, H. Tanaka, *Phys. Rev. Lett.* **2009**, *102*, 108303.
- [65] K. G. F. Janssens, D. Raabe, E. Kozeschnik, M. A. Miodownik, B. Nestler, *Computational Materials Engineering: An Introduction to Microstructure Evolution*, Elsevier/Academic Press, London, UK **2010**.
- [66] K. Luo, *Eur. Polym. J.* **2006**, *42*, 1499.
- [67] H. J. Keh, *Curr. Opin. Colloid Interface Sci.* **2016**, *24*, 13.
- [68] F. Wang, M. Selzer, B. Nestler, *Physica D* **2015**, *307*, 82.
- [69] A. Golovin, A. Nir, L. Pismen, *Ind. Eng. Chem. Res.* **1995**, *34*, 3278.
- [70] I. M. Lifshitz, V. V. Slyozov, *J. Phys. Chem. Solids* **1961**, *19*, 35.
- [71] C. Wagner, *Z. Elektrochem.* **1961**, *65*, 581.
- [72] C. Sternling, L. Scriven, *AIChE J.* **1959**, *5*, 514.
- [73] N. Yan, Y. Sheng, H. Liu, Y. Zhu, W. Jiang, *Langmuir* **2015**, *31*, 1660.
- [74] S. R. Niezgodna, Y. C. Yabansu, S. R. Kalidindi, *Acta Mater.* **2011**, *59*, 6387.
- [75] D. B. Brough, A. Kannan, B. Haaland, D. G. Bucknall, S. R. Kalidindi, *Integr. Mater. Manuf. Innov.* **2017**, *6*, 147.
- [76] R. Bostanabad, Y. Zhang, X. Li, T. Kearney, L. C. Brinson, D. W. Apley, W. K. Liu, W. Chen, *Prog. Mater. Sci.* **2018**, *98*, 1.
- [77] A. Cecen, Y. C. Yabansu, S. R. Kalidindi, *Acta Mater.* **2018**, *158*, 53.
- [78] P. Steinmetz, Y. C. Yabansu, J. Hötzer, M. Jainta, B. Nestler, S. R. Kalidindi, *Acta Mater.* **2016**, *103*, 192.
- [79] Y. C. Yabansu, P. Steinmetz, J. Hötzer, S. R. Kalidindi, B. Nestler, *Acta Mater.* **2017**, *124*, 182.
- [80] Z. Yang, Y. C. Yabansu, R. Al-Bahrani, W.-k. Liao, A. N. Choudhary, S. R. Kalidindi, A. Agrawal, *Comput. Mater. Sci.* **2018**, *151*, 278.
- [81] S. R. Kalidindi, M. De Graef, *Annu. Rev. Mater. Res.* **2015**, *45*, 171.
- [82] A. Çeçen, T. Fast, E. Kumbur, S. Kalidindi, *J. Power Sources* **2014**, *245*, 144.
- [83] A. Cecen, H. Dai, Y. C. Yabansu, S. R. Kalidindi, L. Song, *Acta Mater.* **2018**, *146*, 76.
- [84] P. Altschuh, Y. C. Yabansu, J. Hötzer, M. Selzer, B. Nestler, S. R. Kalidindi, *J. Membr. Sci.* **2017**, *540*, 88.
- [85] L. Ratke, W. K. Thieringer, *Acta Metall.* **1985**, *33*, 1793.